FULL PAPER

Lasing Emission from Plasmonic Nanodome Arrays

Hsin-Yu Wu, Longju Liu, Meng Lu,* and Brian T. Cunningham*

Plasmonic nano-dome arrays (PNDA) have been previously studied as chemical and biological sensors. The present study reports large-area plasmonic lasing from the PNDA structures with liquid-phase gain materials to provide optical gain. The PDNA structure consists of a 2D array of nanoposts, fabricated inexpensively using a nanoreplica molding process, with silicon dioxide and gold thin-film coatings to produce the dome-shaped surface profile. Covered with a dye-doped solution, the PDNA structures can generate lasing emission when they are optically pumped above the lasing threshold. The lasing emission is enabled by energy coupling from the photoexcited dye molecules to the hybridized plasmon mode supported by the PDNA oscillator. Two PDNA lasers with array periods of 400 and 450 nm are fabricated and characterized. Plasmonic resonant modes of the PDNA lasers are numerically studied to illustrate the underlying lasing mechanism. The emission characteristics, including lasing wavelength, linewidth, threshold, beam divergence, and radiation angle, are presented in the paper. The PNDA laser represents a new path for plasmonic lasing in the near-infrared region with potential applications that include integrated photonic circuits, optical communications, and high-performance biosensors.

1. Introduction

Surface plasmon polarizaton (SPP) and localized surface plasmon (LSP) modes supported by metallic nanostructures offer remarkable opportunities for exploration of light-matter interactions at a scale size well below the diffraction limit. The enhanced local electromagnetic fields associated with the plasmon resonance have been adopted for a wide range of applications, including photovoltaic power generation, solid-state lighting, biological and chemical detection, nano-particle trapping, and lasers.[1–11] Among these applications, plasmonic lasers have recently attracted much interest, which can be broadly categorized into two groups: nanoscale plas-

monic resonators and metal-coated 1D/2D arrays. Nanolasers based on plasmonic nano-resonators, such as nanowires on a metal film, gain material-coated metal nanoparticles, and metal-coated semiconductor nanopillars, are designed to exhibit extremely localized volumes of strong fields that spatially overlap the gain media.[12–15] In contrast, plasmonic lasing from periodic arrays of metallic nanostructures occurs at a band-edge plasmon mode with directional emission perpendicular to the device surface.[16–21] However, further detailed study of the lasing action resulting from nonband-edge plasmon modes with directional but nonvertical emission has not been extensively reported.

We recently developed a plasmonic nano-dome array (PNDA), which supports both LSP and SPP Bloch wave (SPP-BW) modes.[22] The PNDA devices have been successfully implemented for biological and chemical detection, such as surface-enhanced Raman scattering and label-free refractometric sensing.[22–26] For a PNDA structure, the LSP mode is generated by the dipole–dipole coupling between the adjacent nano-domes. In contrast, the SPP-BW mode is caused by the periodic structure of the PNDA. Coupled with these plasmon modes, a liquid laser dye solution covering the PNDA structure can produce sufficient optical gain to compensate inherent metal losses, and thus enables laser oscillation. The investigation of how interactions between LSP and SPP-BW modes with the gain material enable lasing action would advance our fundamental knowledge of plasmonic lasers.

This paper reports a plasmonic laser comprised of a dye-doped solution as the gain medium and the PNDA structure as the oscillator, for lasing in the near infrared (NIR). The PDNA device is fabricated using a two-step process that includes nanoreplica molding and the deposition of thin films. The simple fabrication process does not require any type of expensive lithography (such as electron beam lithography, deep-UV lithography, or focused ion beam milling) to create 10–20 nm gap features uniformly over large surface areas. The plasmon resonances of the PNDA laser are numerically studied by finite difference time domain (FDTD) simulation to investigate how the plasmonic resonant modes are related to the laser oscillation. Two PNDA structures with different array periods are designed and fabricated. The key emission features, including lasing wavelength, linewidth, threshold, beam divergence, and radiation angle, are experimentally characterized.

Dr. H.-Y. Wu, Prof. B. T. Cunningham
Department of Electrical and Computer Engineering
Department of Bioengineering
Micro and Nanotechnology Laboratory
University of Illinois at Urbana-Champaign
208 North Wright Street, Urbana, IL 61801, USA
E-mail: wu47@illinois.edu; bcunning@illinois.edu
L. Liu, Prof. M. Lu
Department of Electrical and Computer Engineering
Department of Mechanical Engineering
Iowa State University
2128 Coover Hall, Ames, IA 50011, USA
E-mail: menglu@iastate.edu

www.MaterialsViews.com

ADVANCED
OPTICAL
MATERIALS
www.advopticalmat.de

FULL PAPER

2. Results and Discussion

2.1. Structure of PNDA Laser

Figure 1a shows a schematic illustration of the PNDA laser comprised of a 2D square lattice of gold-coated nano-dome structures, a liquid gain material, and a cover glass window. The nano-dome structure was fabricated by the nanoreplica molding method on a flexible polyethylene terephthalate (PET) substrate and sequentially coated with SiO_2 and Au thin films to complete the periodic PNDA structure over an area of 1.5×1.5 mm². The PNDA structure contains nanoscale gaps between adjacent nano-domes. The nanoreplica molding process is fully described in Figure S1 in the Supporting Information. Two laser dyes (LDS 867 and LDS 765, Exciton Inc.) were dissolved in an organic solvent and the dye solutions were used as the gain media for the PNDA devices with period of $\Lambda = 450$ and $\Lambda = 400$ nm, respectively. As illustrated in Figure 1a, the organic dye solution was excited by ns-laser pulses at an incident angle (θ_i) while emission from the PNDA laser is measured at a detection angle (θ_d). The inset of Figure 1a displays the reciprocal lattice space of a square lattice, with the light gray region indicating the first Brillouin zone while the dark grey region describes the irreducible Brillouin zone. Figure 1b shows a cross-sectional diagram for one period of the PNDA laser, where photons emitted by the photoexcited

dye molecules residing in the vicinity of PNDA surface couple to the hybridized plasmon (HP) mode. Above the lasing threshold, narrowband directional emission emerges when the plasmonic losses are overcome by the optical gain. Scanning electron microscopy (SEM) images in Figure 1c,d show the top-view surface profiles of the fabricated PNDA structures with period of $\Lambda = 450$ and $\Lambda = 400$ nm, respectively.

2.2. Plasmonic Resonant Modes of the PNDA Laser

To investigate the effects of plasmon resonances of the PNDA laser on the lasing action, we experimentally and numerically characterize the extinction spectra of the PNDA laser ($\Lambda = 450$ nm). The extinction spectrum measured at normal incidence for *p*-polarized illumination is shown as the red curve in **Figure 2**a. The measured spectrum matches well with the computer-simulated spectrum, which is calculated using the FDTD method (Lumerical Solutions, Inc.), plotted as the blue curve. The extinction spectra exhibited two distinct plasmon resonance peaks, which are labeled by the orange and magenta dots. The modes associated with the indicated plasmon resonances are assigned to the SPP-BW mode with a narrow resonance linewidth at $\lambda_{SPP-BW} = 625$ nm and the dipole LSP mode with a broad feature at $\lambda_{LSP} = 931$ nm. A small resonance
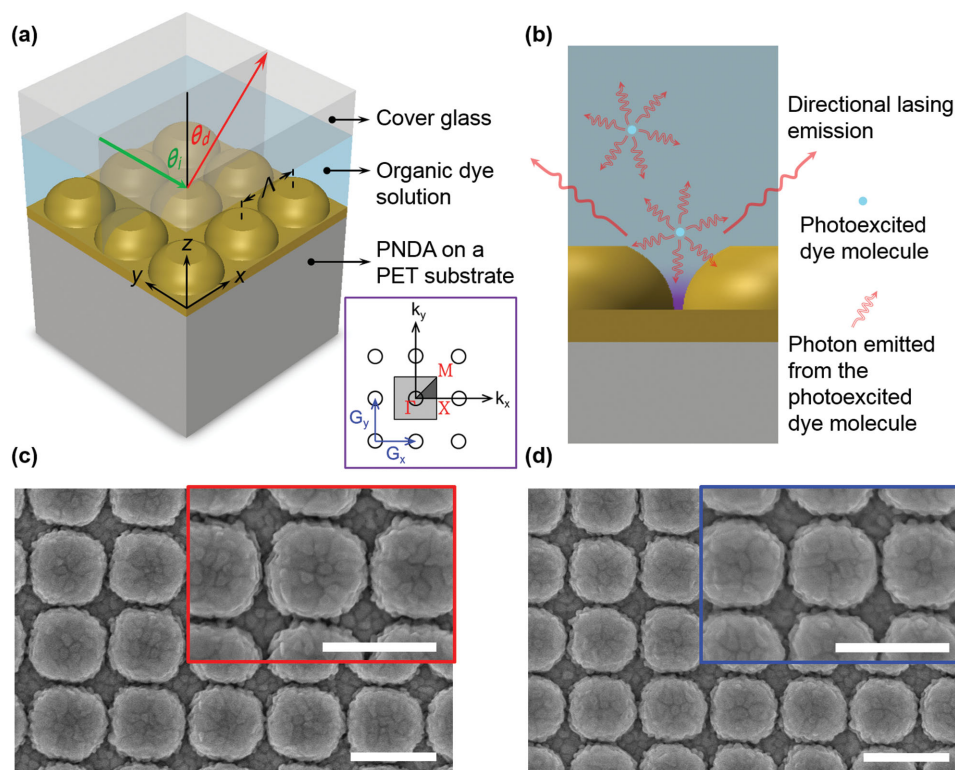
Figure 1. PNDA laser. a) Schematic of the 2D square lattice of the PNDA laser. An organic dye solution, sandwiched between the PNDA structure and a cover glass, is used as a gain medium. Green and red arrows represent the 532 nm pump beam at the incident angle (θ_i) and lasing emission at the detection angles (θ_d), respectively. Inset: the corresponding reciprocal lattice (circles) with the irreducible Brillouin zone (1/8 of the first Brillouin zone), indicated by the dark gray region. b) Schematic of the lasing action for one unit cell of the PNDA laser. Optical excitation at 532 nm creates photoexcited dye molecules in the gain material and the emission of the dye molecules couples to the HP mode via the near-field interaction. Top-view SEM images of the fabricated PNDA surfaces with period of c) $\Lambda = 450$ and d) $\Lambda = 400$ nm on a flexible plastic substrate. Inset: SEM close-up views of the PNDA surfaces showing inter-dome separation distance of 15 nm. Scale bars = 500 nm.

© 2016 WILEY-VCH Verlag GmbH & Co. KGaA, Weinheim
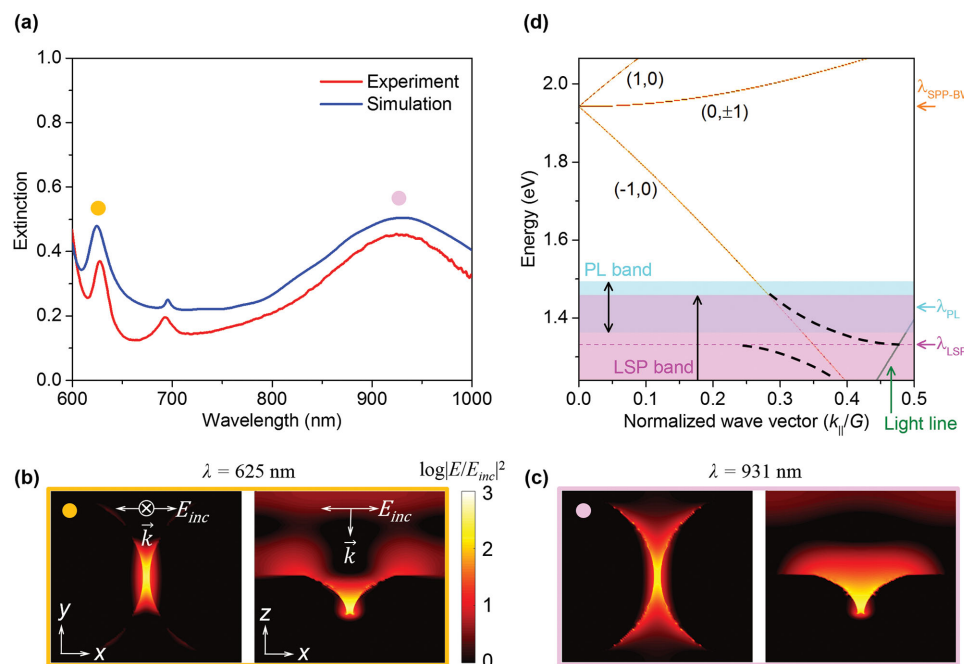
Figure 2. Optical characteristics of the PNDA laser (Λ = 450 nm; LDS 867 in methanol). a) Extinction spectra of the PNDA laser under normal incidence for *p*-polarized illumination along the Γ–*X* direction of the PNDA laser (red curve: experimentally measured extinction spectrum; blue curve: spectrum obtained by FDTD simulation). b,c) Top and cross-sectional views of the spatial electric-field intensity enhancement distribution associated with indicated b) SPP-BW mode and c) LSP mode for one unit cell volume of the PNDA laser. The middle color bar represents the resonant electric field intensity ($|E|^2$) normalized with respect to the incident electric field intensity ($|E_{inc}|^2$) on a logarithmic scale. d) Calculated dispersion of SPP-BW modes with magenta- and cyan-colored areas representing LSP and PL bands, respectively. Black dashed curves indicate anti-crossing behavior due to hybridization of the LSP and SPP-BW modes.

observed at 696 nm is attributed to the SPP-BW at the interface between metal and the underlying SiO$_2$ film. These modes can be identified by the distributions of their surface charge and near field.[22] Figure 2b,c shows the top-view (*x*–*y* plane) and cross-sectional view (*x*–*z* plane) of spatial electric-field intensity enhancement profiles within one unit volume of the PNDA laser for the SPP-BW and the LSP modes, respectively. The color bar in the middle is scaled by the normalization of electric field intensity ($|E|^2$) to the incident electric field intensity ($|E_{inc}|^2$) on a logarithmic scale. Both resonant modes exhibit the most intense electric-field intensity confined within the nano-gaps between the adjacent nano-domes. The strongly confined resonant modes spatially overlap the superstrate gain medium residing inside the gap. It is noteworthy that the spectral position of the LSP mode is insensitive to the angle of incidence and can be determined by the inter-dome separation, the material properties, dome diameter and height, and partially by the lattice constant.[27,28] Unlike the dispersionless LSP mode, the SPP-BW mode exhibits strong dispersion, which is given by the Bragg coupling equation[29,30]

$$\frac{\omega}{c}\sqrt{\frac{\varepsilon_m \varepsilon_d}{\varepsilon_m + \varepsilon_d}} = \left| k_\parallel + pG_x + qG_y \right| \tag{1}$$

where ω and c are respectively the angular frequency and speed of free-space light, ε_m and ε_d are respectively the relative permittivities of the metal and the gain solution, $k_\parallel$ is the in-plane wave vector of incident light, G_x and G_y are reciprocal vectors ($|G_x| = |G_y| = 2\pi/\Lambda = |G|$), shown in the inset of Figure 1a, and

integer index pairs (*p*, *q*) specify the order of SPP-BW modes. The calculated dispersion of SPP-BW modes for $k_\parallel$ along the Γ–*X* direction are depicted as the orange/yellow curves of Figure 2d, marked by (1, 0), (0, ±1) and (–1,0). For a square lattice, all four lowest order Bragg vectors, pG_x+qG_y, have the same magnitude. Correspondingly, the four lowest order SPP-BW modes are degenerate modes at normal incidence ($k_\parallel$ = 0). When the $k_\parallel \neq 0$, the mirror symmetry of the square lattice requires that the SPP wave vectors (k_{SPP}) of the (0, 1) and (0, –1) modes have the same magnitude. Consequently, the (0, 1) and (0, –1) modes are degenerated in the band diagram shown in Figure 2d. As the normalized wave vector increases from ≈0.28, the (–1, 0) SPP-BW mode spectrally overlaps with the broad LSP band (850–1010 nm; the area colored in magenta) with the extinction maximum located at λ_{LSP} = 931 nm. The dispersion relation of two strongly coupled modes shows an anti-crossing behavior (black dashed curves) where new HP modes form as a result of hybridization of the LSP and SPP-BW modes.[31]

In periodic arrays of metallic nanostructures, the lasing action usually occurs at the high symmetry points within the first Brillouin zone. The band-edge mode at the Γ-point reveals a group velocity ($v_g = \partial\omega/\partial k_{//}$) near zero, and a slow light effect that can strongly enhance the interaction of light and the gain material.[18] The Γ band-edge of the (0, ±1) plasmon mode, which spectrally overlaps the photoluminescence (PL) band of the gain material, have been utilized to produce lasing emission normal to the device surface.[20] Since the spectral position of the PL band of the laser dye determines which plasmon mode is selected for laser oscillation, the PNDA laser (Λ = 450 nm)

www.MaterialsViews.com

**ADVANCED
OPTICAL
MATERIALS**

www.advopticalmat.de

FULL PAPER

utilizes a laser dye (LDS 867) solution with a PL band in the NIR region (830–910 nm; the cyan-colored area) with emission maximum centered at $\lambda_{PL} = 870$ nm. The PL band of the laser dye spectrally overlaps the upper energy branch of the HP modes, represented by the upper black dashed curve in Figure 2d, with a decreased group velocity as the in-plane wave vector $k_\parallel$ increases, allowing photons emitted by the photo-excited dye molecules to couple into the upper HP mode via the near-field interaction. Because the HP mode always lies inside the radiation continuum, the photons are subsequently radiated into free space at the angle that matches the in-plane wave vector of the HP mode. Laser oscillation occurs once the optical gain provided by the gain medium can balance the material and radiation loss of the HP mode. The spatial electric-field intensity enhancement profile at the lasing condition ($\lambda_{lasing} = 907$ nm and $\theta = 50°$) is given in Figure S2 in the Supporting Information.

2.3. Lasing Action of the PNDA Laser

Characterization of lasing emission was carried out by optically pumping the PNDA laser using a frequency-doubled Nd:YAG pulse laser ($\lambda_{pump} = 532$ nm; pulse width = 10 ns; repetition rate = 2 Hz). Details of the measurement are described in the experimental section and the apparatus is schematically illustrated in Figure S3 in the Supporting Information. This section presents the measured lasing characteristics, including spectral, polarization and angular properties.

2.3.1. Lasing Threshold

Figure 3a shows typical emission spectra of the PNDA laser ($\Lambda = 450$ nm) recorded at $\theta_d = 50°$ for emission parallel (red curve) and perpendicular (blue curve) to the plane of incidence. The lasing emission spectra are compared with the PL spectrum of LDS 867. The PL spectrum (green curve) was measured on a planar surface coated with a gold film. The PL spectrum is broad with a full-width at half-maximum (FWHM) of ≈60 nm centered at $\lambda_{PL} = 861$ nm. When the PNDA laser ($\Lambda = 450$ nm) was optically pumped with a fluence of 0.89 mJ cm^{-2}, a narrow

and intense laser oscillation occurred at $\lambda_{lasing} = 907$ nm with a FWHM of 2.73 nm. The lasing emission peak appears at a longer wavelength with respect to the PL profile of the dye solution. Because the lattice arrangement of PNDAs is symmetrical along the x- and y-directions, the emission is polarization-independent and therefore the vertically and horizontally polarized components exhibited nearly identical spectral profiles. In Figure 3b, we plot the recorded emission spectra as a function of pump fluence. By increasing the pump fluence above a critical value, the emission intensity at $\lambda_{lasing} = 907$ nm increases dramatically and the emission linewidth decreases. The inset of Figure 3b summarizes peak intensity at $\lambda_{lasing} = 907$ nm as a function of the pump fluence. The input–output relationship shows the characteristic threshold behavior. A clear threshold fluence of approximately 0.32 mJ cm^{-2} is observed. Above the threshold, the laser output rises linearly with pump fluence.

To study emission characteristics of the PNDA laser with $\Lambda = 400$ nm, a different gain material (LDS 765) with a PL spectrum shown in **Figure 4**a was chosen to improve spectral overlap between the gain medium and the upper HP mode of the PNDA laser ($\Lambda = 400$ nm). Figure 4a shows a typical emission spectrum of the PNDA laser ($\Lambda = 400$ nm) measured under a pump fluence of 0.63 mJ cm^{-2} at $\theta_d = 50°$. The lasing emission peak locates at the long wavelength tail of the PL curve with $\lambda_{lasing} = 807$ nm with a FWHM of 2.53 nm. At the lasing wavelength, the emission intensity is three orders of magnitude stronger than the background PL signal. The evolution of the emission spectra as a function of pump fluence is shown in Figure 4b to validate the lasing action. A clear laser threshold is observed at pump fluence of approximately 0.3 mJ cm^{-2}, as shown in the inset of Figure 4b.

2.3.2. Radiation Pattern

The lasing emission is strongly angular-dependent and is determined by the plasmon modes, which are determined by the band structure of the PNDA laser. To investigate the correlation, angle-resolved emission measurements were carried out to study the radiation pattern. The emission spectra measured at 70 different detection angles, ranging from 10° to 80°, were recorded and shown in **Figure 5**a,b for the PNDA lasers
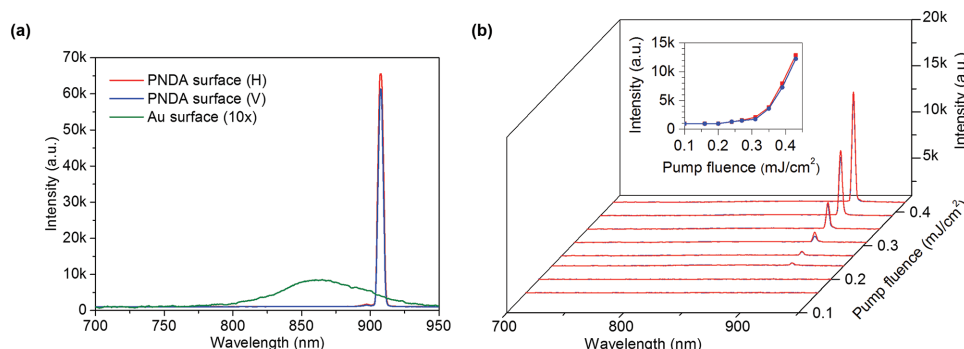
Figure 3. Lasing characteristics of the PDNA laser with $\Lambda = 450$ nm. a) Comparison of emission spectra of the PNDA laser and emission spectrum for the same gain material (LDS 867 doped methanol) on a planar gold surface, i.e., the PL of LDS 867. H (red) and V (blue) respectively represent emission polarized parallel and perpendicular to the lattice direction (Γ–X) of the PNDA laser. b) Evolution of lasing emission spectra for different pump fluences and emission polarizations. Inset: peak intensity as a function of pump fluence for different emission polarizations.
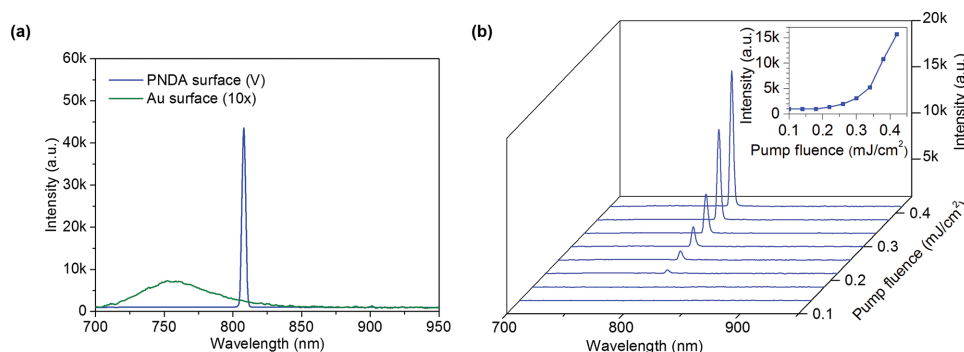
Figure 4. Lasing characteristics of the PDNA laser with Λ = 400 nm. a) Comparison of emission spectrum of the PNDA laser and emission spectrum for the same gain material (LDS 765 doped methanol) on a flat gold surface without nanostructured patterning. V (blue) represents emission polarized perpendicular to the lattice direction (Γ–X) of the PNDA laser. b) Evolution of lasing emission spectra for different pump fluences. Inset: peak intensity as a function of pump fluence.

with Λ = 450 and 400 nm, respectively. The incident angle of the pump beam was fixed at 0° and pump fluence was kept at 0.89 and 0.63 mJ cm^{-2}, respectively, which are well above the lasing threshold for both devices. The position of the detector was scanned as illustrated in Figure S3 in the Supporting Information. Each slice on the vertical axis represents the emission spectrum measured at a particular detection angle (θ_d). Although both devices exhibit intense lasing emission near 50°, their lasing wavelengths are different. Figure 5a,b represents the s-polarized lasing emission, where the electric field of the emission is perpendicular to the plane of incidence. Owing to the symmetric arrangement of the PNDA structure, the

p-polarized lasing emission exhibits a nearly identical pattern as shown in Figure S4 in the Supporting Information. Figure 5c plots the lasing emission intensities as a function of detection angle (θ_d) defined in Figure S3 in the Supporting Information. The divergence angle ($\Delta\theta_d$) of the lasing beam is 1.46° measured on the plane parallel to the high symmetry direction. In short, the threshold behavior in combination with the narrow emission linewidth as well as small beam divergence demonstrates that room-temperature laser oscillation occurs in PNDA lasers. It is worth noting that several relatively weak emissions exist away from the main lobe. We suggest this phenomenon is related with the LSP mode supported by the nano-gaps formed
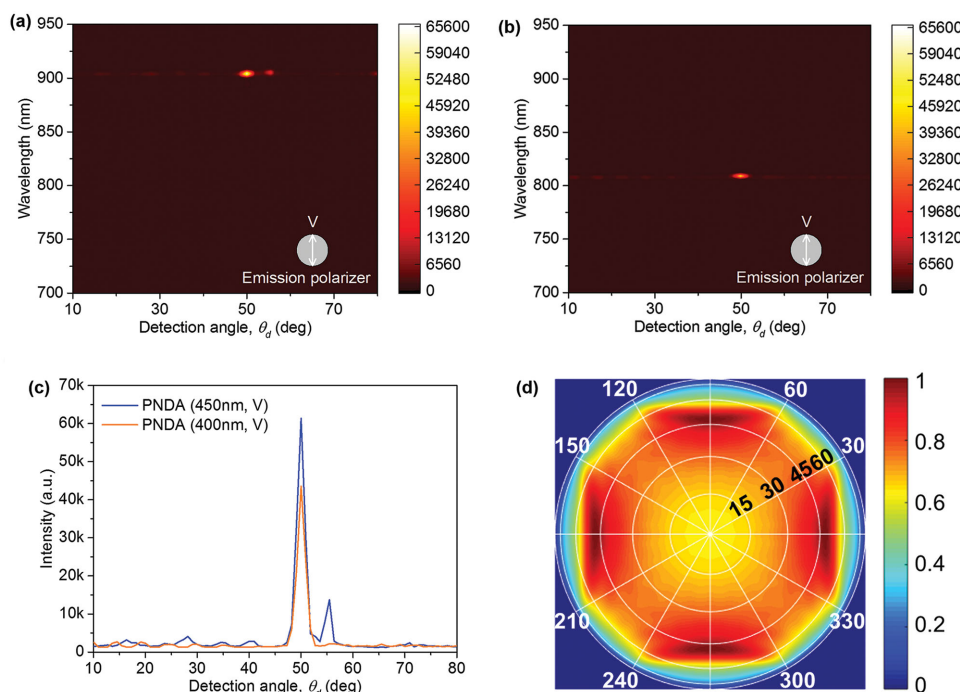
Figure 5. Angular dependence of the lasing emission. Measured angular emission spectra of a) the PNDA laser (Λ = 450 nm; LDS 867 in methanol) and b) the PNDA laser (Λ = 400 nm; LDS 765 in methanol) at a fixed incident angle (θ_i = 0°) as a function of detection angle (θ_d) for emission polarized perpendicular (V) to the lattice direction (Γ–X) of the PNDA laser. c) The angular emission profiles for the spectral wavelength of λ_{lasing} = 907 nm in (a) and λ_{lasing} = 807 nm in (b). d) Simulated angular distribution of far-field emission of the PNDA laser (Λ = 450 nm) at λ = 905 nm. The black characters represent the polar angle (θ) and the white the azimuthal angle (ϕ).

between the adjacent nano-domes because the weak emissions are observed in all directions in the range of 10°–80°.

The out-of-plane radiation angles θ can be found using: $k_0 \sin\theta = k_\parallel = G/(2n_{eff})$, where $k_0 = 2\pi/\lambda_0$ is the free-space wave vector of the out-coupled laser radiation, $k_\parallel$ is the in-plane wave vector, G is the lattice vector ($2\pi/\Lambda$) and n_{eff} is the effective refractive index. n_{eff} is estimated to be 1.33 for both laser dyes and therefore the lasing action, arising from the interaction of the liquid gain medium and the HP mode, occurs at the condition of $k_\parallel/G = 1/(2n_{eff}) = 0.376$, where the optical gain is sufficient to overcome the losses inherent in the plasmonic material, as shown in Figure 2d. The lasing emission angle is calculated to be $\approx 49°$ for both laser dyes by using the value of $k_\parallel$ together with the measured lasing wavelengths, which is in good agreement with the measurements, as shown in Figure 5c. Figure 5d shows the simulated angular distribution of far-field emission of the PNDA laser ($\Lambda = 450$ nm) at $\lambda = 905$ nm for randomly placed and oriented dipoles. Strong emission can be clearly seen at $\theta \approx 50°$ with the azimuthal angle of $\phi = 0°$, 90°, 180°, and 270°, respectively. Because the square lattice of the PNDA is symmetric, there are four high symmetry $\Gamma-X$ directions along $\pm k_x$ and $\pm k_y$ in $\mathbf{k}$ space. In the experiment, although the detection angle (θ_d) was varied along one of $\Gamma-X$ directions, we expect to observe the lasing emissions at $\theta_d = \pm 50°$ in both x–z and y–z planes shown in Figure 1a.[32] In addition, we also studied how the incident angle of the pulse laser affects the lasing emission using the setup illustrated in Figure S5 in the Supporting Information. The result shown in Figure S6 in the Supporting Information indicates that lasing emission is independent of the incident angle of the excitation beam.

3. Conclusion

In summary, a liquid dye plasmonic laser has been successfully demonstrated. Two PNDA lasers with different dimensions and liquid gain materials were designed, fabricated, and characterized. Owing to the strong local field near the PDNA surfaces, the gain within the liquid dye can exceed the loss inherent within plasmonic resonant structures and thus room-temperature lasing emission can be achieved at a low threshold fluence. For the PNDA laser with a period of 450 nm, laser oscillation occurred at 907 nm and showed a clear lasing threshold near 0.32 mJ cm^{-2}. The PDNA laser with a period of 400 nm operated at 807 nm and revealed a threshold pump fluence of ≈ 0.3 mJ cm^{-2}. The period of the PNDA structure can be engineered to tune the hybridized plasmon resonance and consequently determine the lasing wavelength of the plasmonic laser. Directional lasing emissions over large areas were observed for both PNDA lasers at off-normal direction ($\theta_d = 50°$) with a small divergence angle ($\Delta\theta_d < 1.5°$). Compared to other types of plasmonic lasers, the PNDA laser offers several beneficial features: (i) The PNDA laser is fabricated using a low-cost, room-temperature nanoreplica molding process on a flexible substrate and thus the device is amendable to scale up over large surface areas and flexible materials. (ii) The PNDA laser can implemented by combining the PDNA structure with a wide variety of gain materials, such as quantum dots, light emitting polymer, and fluorescence proteins. (iii) The dimension of PDNA structure

can be engineered to produce plasmonic lasing at any wavelength in the visible and near-infrared region, provided that the PL band of the gain material is selected to spectrally overlap the HP mode. (iv) Unlike the band-edge lasing devices, where emissions toward an off-normal direction to the device surface are inhibited, the emission of the PNDA laser can be directed obliquely. We envision that the PNDA structure can be utilized in integrated photonic systems as a coherent light source or in lab-on-a-chip applications as high-performance chemical and biological sensors.

4. Experimental Section

Fabrication of PNDA Lasers: The schematic diagram of the replica molding process utilized to fabricate the nano-dome structure is summarized in Figure S1 in the Supporting Information. This low-cost, large-area, and high-throughput fabrication method was comprehensively described in our previous publications.[22,33] The organic dyes (LDS 867 and LDS 765, Exciton Inc.) were dissolved in methanol at a concentration of 100×10^{-6} M. The dye solutions were filtered using a 0.2 µm syringe filter to remove undissolved particles. A chamber was formed between the PNDA substrate and a cover glass window, using a layer of double sided pressure sensitive adhesive film with a thickness ≈200 µm (3 M). The chamber was filled with the filtered dye solution with a volume of 5 µL.

Reflection Measurement and Extinction Spectrum: Reflection measurement of the PNDA laser was carried out using an Axio Observer D1 inverted microscope (Carl Zeiss, Inc.) equipped with a 100 W halogen light source. The p-polarized incident broadband light was focused onto the PNDA surface via a 10× objective (NA = 0.25) and the reflected light was collected back through the same objective and then coupled to a visible and near-infrared (Vis–NIR) spectrometer (Control Development, Inc.) through an optical fiber. Reflectance (R) was calculated against a mirror-like Au film covered with the LDS solution over microscope glass slide as the reference. Extinction spectra were obtained by calculating $1 - R$.

Numerical Modeling: 3D FDTD simulations were performed to simulate the optical responses of PNDA laser using a commercial software package (FDTD solution, Lumerical Inc.). The PNDA structure was illuminated with a normally incident, unit magnitude plane wave propagating in the −z direction with an electric field polarization along the x-axis. The simulation region was set to one unit cell volume of the periodic PNDA structure along with periodic boundary conditions imposed on the sidewalls of the simulation boundary. Perfectly matched layer (PML) boundary conditions were imposed at boundaries along the z direction to properly absorb incident radiation. Monitors were placed in close proximity to PMLs to calculate the amount of reflected and transmitted power as a function of wavelength. A uniform fine mesh size of 1 nm (x, y, and z directions) was used within the nanogap region. The optical properties of Au and SiO$_2$ were respectively taken from Johnson and Christy and Palik's handbook, and then fit by the multi-coefficient model in the wavelength range from 600 to 1000 nm. The material dispersion of superstrate gain material and plastic substrate were ignored in the simulation.

Laser Emission Measurement Setup: A schematic illustration of the optical setup for laser emission characterization is shown in Figure S3 in the Supporting Information. The PNDA laser was optically pumped by a frequency-doubled, Q-switched Nd:YAG pulse laser (Minilite, Continuum) with emission wavelength of 532 nm and pulse duration of 10 ns at a repetition rate of 2 Hz. Pump spot size and fluence were varied by an adjustable iris and a continuous variable neutral density (ND) filter. A half-wave plate was used to rotate the polarization of the pump laser so that the incident plane of the pump laser was aligned along the high symmetry axis of the square lattice. The PNDA device was mounted on a fixed sample holder. The p-polarized pump pulses were incident on the surface of PNDA laser with a measured spot size of 1 mm diameter

at normal incidence ($\theta_i = 0°$). The laser emission was collected by a NIR doublet lens (NA = 0.25) mounted on a computer-controlled custom stage that can be rotate over a range of detection angles ($\theta_d = 10–80°$) in increments of 1° with respect to the device surface normal. The collected light was coupled to a Vis–NIR multimode fiber, which was connected to a spectrometer (USB2000+, Ocean Optics) with a spectral resolution of 0.3 nm. A linear polarizer was placed in front of the doublet lens to characterize the polarization of laser emission.

Supporting Information

Supporting Information is available from the Wiley Online Library or from the author.

Acknowledgements

[1] A. G. Brolo, *Nat. Photonics* **2012**, *6*, 709.

[2] H. A. Atwater, A. Polman, *Nat. Mater.* **2010**, *9*, 205.

[3] C. Min, Z. Shen, J. Shen, Y. Zhang, H. Fang, G. Yuan, L. Du, S. Zhu, T. Lei, X. Yuan, *Nat. Commun.* **2013**, *4*, 2891.

[4] M. W. Kim, P. C. Ku, *Appl. Phys. Lett.* **2011**, *98*, 201105.

[5] P. Berini, I. De Leon, *Nat. Photonics* **2012**, *6*, 16.

[6] G. Lozano, D. J. Louwers, S. R. K. Rodriguez, S. Murai, O. T. A. Jansen, M. A. Verschuuren, J. G. Rivas, *Light Sci. Appl.* **2013**, *2*, e66.

[7] H. Gao, W. Zhou, T. W. Odom, *Adv. Funct. Mater.* **2010**, *20*, 529.

[8] H. Gao, J. Henzie, M. H. Lee, T. W. Odom, *Proc. Natl. Acad. Sci. USA* **2008**, *105*, 20146.

[9] R. F. Oulton, V. J. Sorger, T. Zentgraf, R. M. Ma, C. Gladden, L. Dai, G. Bartal, X. Zhang, *Nature* **2009**, *461*, 629.

[10] H.-Y. Wu, B. T. Cunningham, *Appl. Phys. Lett.* **2011**, *98*, 153103.

[11] M. Zhang, M. Lu, C. Ge, B. T. Cunningham, *Opt. Express* **2014**, *22*, 20347.

[12] J. Y. Suh, C. H. Kim, W. Zhou, M. D. Huntington, D. T. Co, M. R. Wasielewski, T. W. Odom, *Nano Lett.* **2012**, *12*, 5769.

[13] Q. Ding, A. Mizrahi, Y. Fainman, V. Lomakin, *Opt. Lett.* **2011**, *36*, 1812.

[14] D. J. Bergman, M. I. Stockman, *Phys. Rev. Lett.* **2003**, *90*, 027402.

[15] M. Khajavikhan, A. Simic, M. Katz, J. H. Lee, B. Slutsky, A. Mizrahi, V. Lomakin, Y. Fainman, *Nature* **2012**, *482*, 204.

[16] P. Andrew, G. A. Turnbull, I. D. W. Samuel, W. L. Barnes, *Appl. Phys. Lett.* **2002**, *81*, 954.

[17] F. van Beijnum, P. J. van Veldhoven, E. J. Geluk, M. J. A. de Dood, G. W. 't Hooft, M. P. van Exter, *Phys. Rev. Lett.* **2013**, *110*, 206802.

[18] W. Zhou, M. Dridi, J. Y. Suh, C. H. Kim, D. T. Co, M. R. Wasielewski, G. C. Schatz, T. W. Odom, *Nat. Nanotechnol.* **2013**, *8*, 506.

[19] X. Meng, J. Liu, A. V. Kildishev, V. M. Shalaev, *Laser Photonics Rev.* **2014**, *8*, 896.

[20] A. Yang, T. B. Hoang, M. Dridi, C. Deeb, M. H. Mikkelsen, G. C. Schatz, T. W. Odom, *Nat. Commun.* **2015**, *6*, 6939.

[21] C. Zhang, Y. Lu, Y. Ni, M. Li, L. Mao, C. Liu, D. Zhang, H. Ming, P. Wang, *Nano Lett.* **2015**, *15*, 1382.

[22] H.-Y. Wu, C. J. Choi, B. T. Cunningham, *Small* **2012**, *8*, 2878.

[23] H.-Y. Wu, B. T. Cunningham, *Nanoscale* **2014**, *6*, 5162.

[24] C. J. Choi, Z. D. Xu, H.-Y. Wu, G. L. Liu, B. T. Cunningham, *Nanotechnology* **2010**, *21*, 415301.

[25] C. J. Choi, H.-Y. Wu, S. George, J. Weyhenmeyer, B. T. Cunningham, *Lab Chip* **2012**, *12*, 574.

[26] C. J. Choi, S. Semancik, *Nanoscale* **2013**, *5*, 8138.

[27] M. Sarkar, M. Besbes, J. Moreau, J.-F. Bryche, A. Olivéro, G. Barbillon, A.-L. Coutrot, B. Bartenlian, M. Canva, *ACS Photonics* **2015**, *2*, 237.

[28] S. R. K. Rodriguez, A. Abass, B. Maes, O. T. A. Janssen, G. Vecchi, J. Gómez Rivas, *Phys. Rev. X* **2011**, *1*, 021019.

[29] T. W. Ebbesen, H. J. Lezec, H. F. Ghaemi, T. Thio, P. A. Wolff, *Nature* **1998**, *391*, 667.

[30] H. F. Ghaemi, T. Thio, D. E. Grupp, T. W. Ebbesen, H. J. Lezec, *Phys. Rev. B* **1998**, *58*, 6779.

[31] W. Zhou, J. Y. Suh, Y. Hua, T. W. Odom, *J. Phys. Chem. C* **2013**, *117*, 2541.

[32] M. Meier, A. Dodabalapur, J. A. Rogers, R. E. Slusher, A. Mekis, A. Timko, C. A. Murray, R. Ruel, O. Nalamasu, *J. Appl. Phys.* **1999**, *86*, 3502.

[33] Y. Tan, C. Ge, A. Chu, M. Lu, W. Goldshlag, C. S. Huang, A. Pokhriyal, S. George, B. T. Cunningham, *IEEE Sens. J.* **2012**, *12*, 1174.